Supporting Information

Energy-Efficient NbOx/ZrO2 Bilayer Memristor Enabling Low-Voltage Multilevel Switching for Neuromorphic Computing

*Muhammad Wajid Zulfiqar[1,2,3], Sobia Nisar[4], Rimsha Zulfiqar[5], Muneeb Ahmad[2,3], Muhammad Rabeel[3], Hammad Ghazanfar[2,3], Saikh Mohammad Wabaidur[6], Aamir Rasheed[7], Honggyun Kim[3], Ghulam Dastgeer[*8], Deok-kee Kim[*2,3]*

[1]*Department of Optical Engineering, Sejong University, Seoul 05006, Republic of Korea.*

[2]*Department of Convergence Engineering for Intelligent Drone, Sejong University, Seoul 05006, Republic of Korea.*

[3]*Department of Semiconductor Systems Engineering, Sejong University, Seoul, 05006, Republic of Korea.*

[4]*Department of Electrical Engineering and Convergence Engineering for Intelligent Drone, Sejong University, Seoul 05006, Republic of Korea.*

[5]*Department of Chemistry, Riphah International University, Faisalabad, 44000, Pakistan.*

[6]*Department of Chemistry, College of Science, King Saud University, P.O. Bo x 2455, Riyadh, 11451, Saudi Arabia.*

[7]*Department of Chemistry, University of Ulsan, Ulsan, 44610, Republic of Korea*

[8]*Department of Physics and Astronomy, Sejong University, Seoul, 05006, Republic of Korea.*

***Corresponding authors**: Ghulam Dastgeer and Deok-kee Kim*

Email: *gdastgeer@sejong.ac.kr & Deokkeekim@sejong.ac.kr*

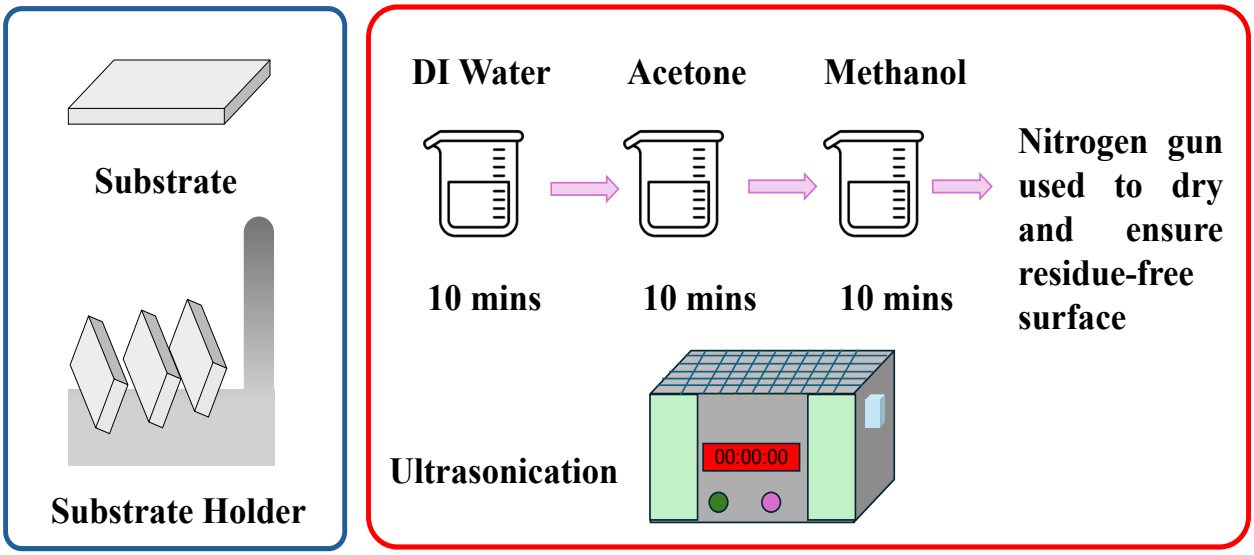

Figure S1: Schematic illustration of the substrate cleaning procedure. The substrates were sequentially cleaned in deionized (DI) water, acetone, and methanol for 10 min each under ultrasonic conditions, followed by drying with a nitrogen gun.

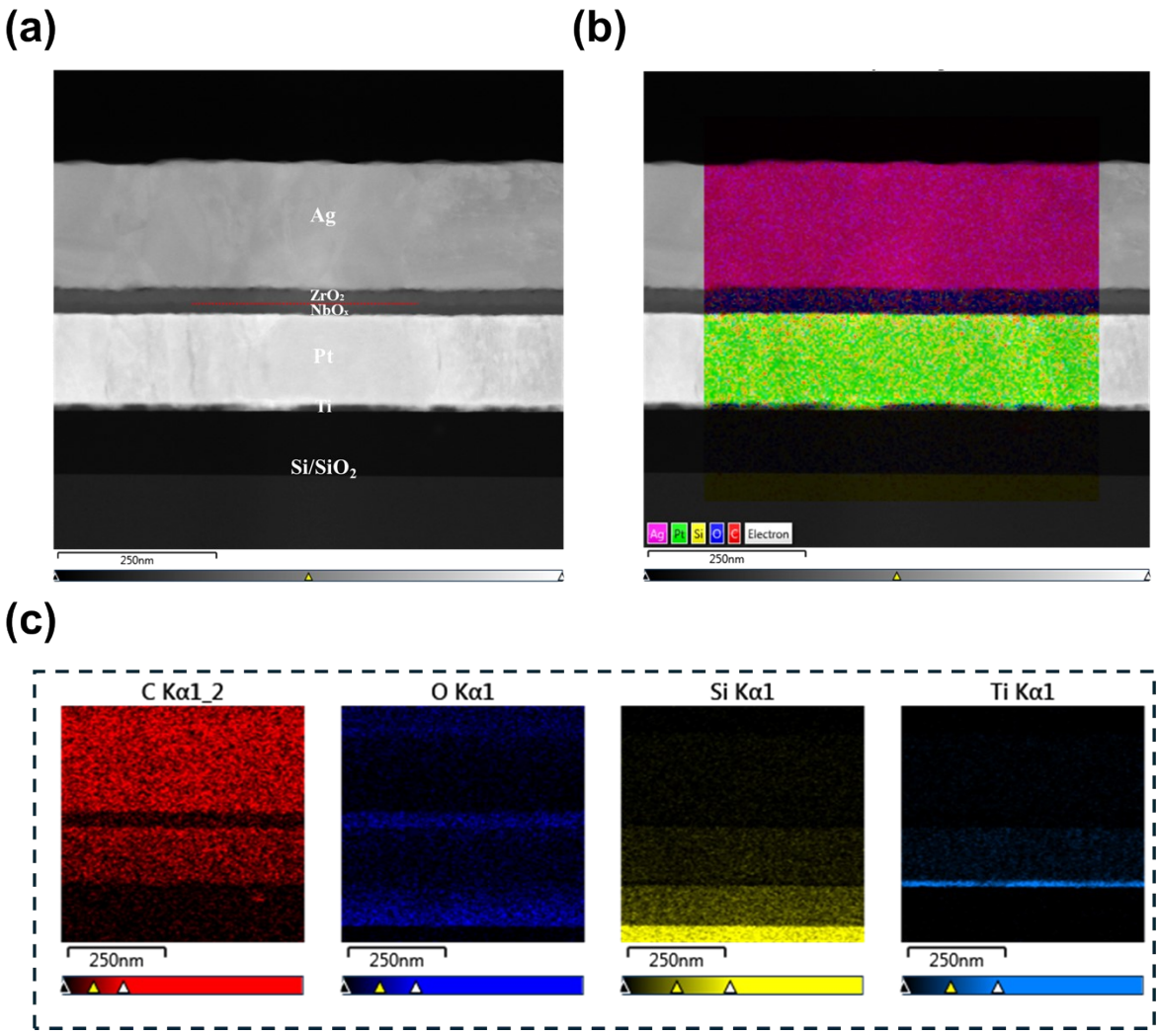

Figure S2: **(a-c)** Cross-sectional TEM image and corresponding EDS elemental mapping of the $Si/SiO_2/Pt/NbO_x/ZrO_2/Ag$ device structure. The images confirm the well-defined bilayer stack with sharp interfaces, where Ag, Zr, Nb, Pt, and Si are clearly distinguished in the elemental maps, validating the uniform deposition and layer integrity.

The XPS spectrum of C1s for the ZrO_2 and NbOx, where the main peak at ~284.6 eV corresponds to C-C/C-H, commonly observed due to surface hydrocarbon contamination. The second component at ~286.1 eV is attributed to C-O/C-OH bonding, indicating the presence of hydroxyl or ether groups. The third peak at ~288.4 eV is assigned to O-C=O species, such as carboxyl or carbonate groups is likely due to surface-adsorbed CO_2. These components confirm the surface chemical heterogeneity and ambient exposure effects on the sample.

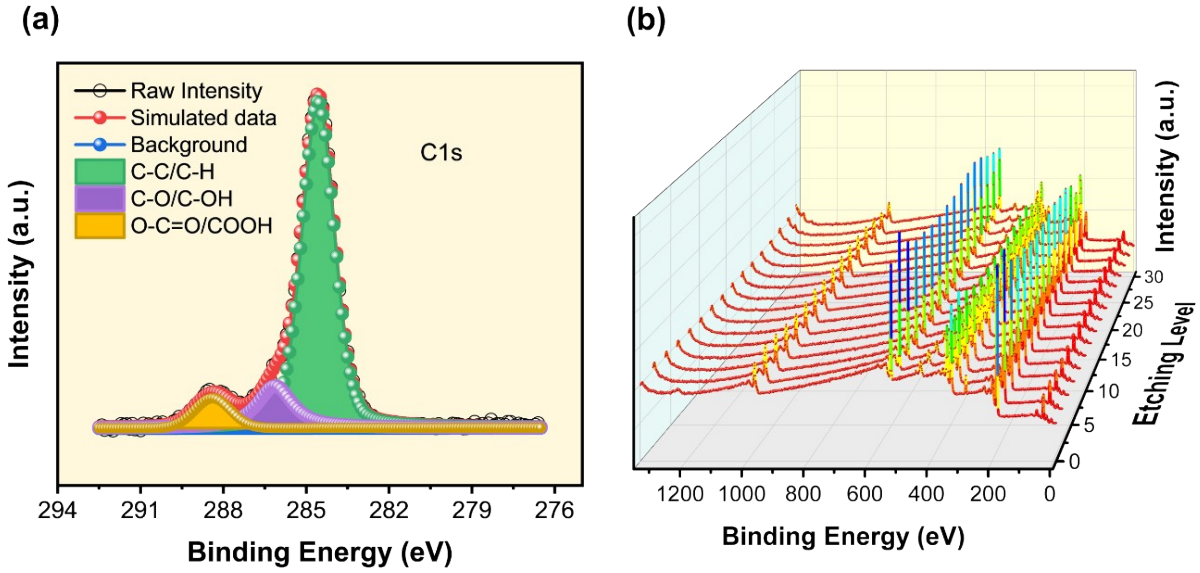

Figure S3: (a) High-resolution XPS spectrum of C1s for the ZrO_2 and NbOx sample. The deconvoluted spectrum indicates the presence of adventitious carbon and surface-adsorbed oxygen-containing species. (b) XPS survey spectra recorded during sequential etching for depth profiling. The variation in elemental peak intensities reflects the compositional evolution across the layered structure.

Single-layer devices exhibit larger variability in their SET and RESET characteristics. A statistical comparison was performed on 11 individual devices for each structure ($Pt/ZrO_2/Ag$ and Pt/NbOx/Ag).

The electroforming behavior of each device is also included for completeness.

For Pt/ZrO2/Ag (>10 Devices)

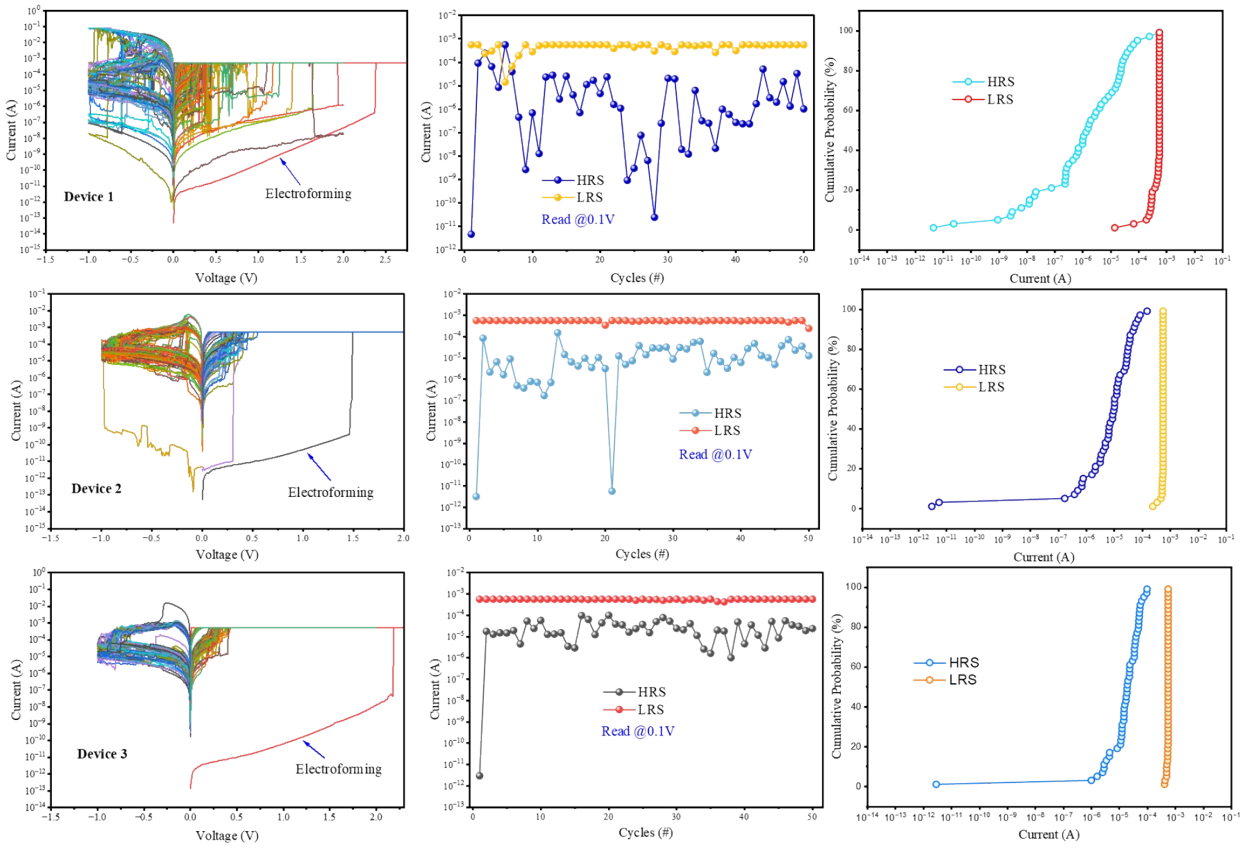

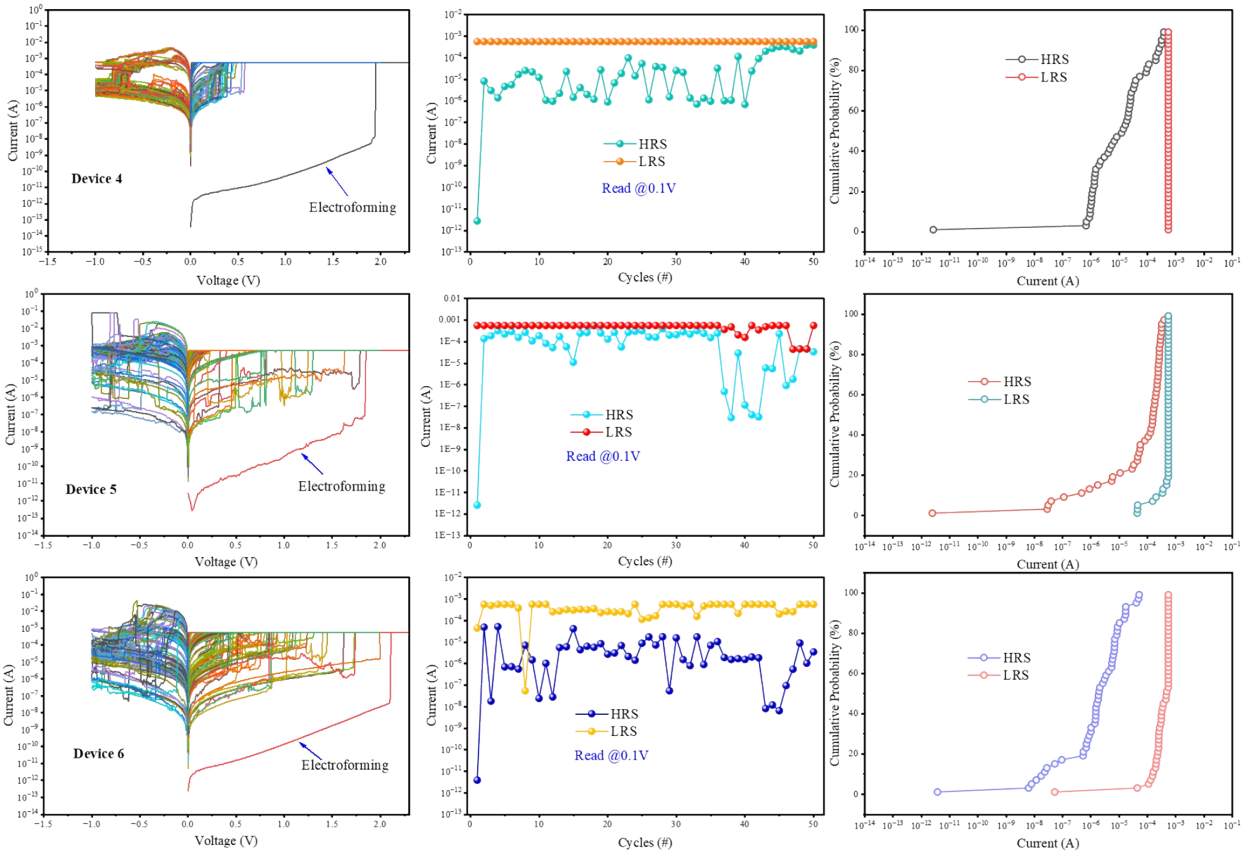
Device 4
Electroforming
Current (A)
Voltage (V)
HRS
LRS
Read @0.1V
Cycles (#)
Cumulative Probability (%)
Current (A)
Device 5
Electroforming
Device 6
Electroforming

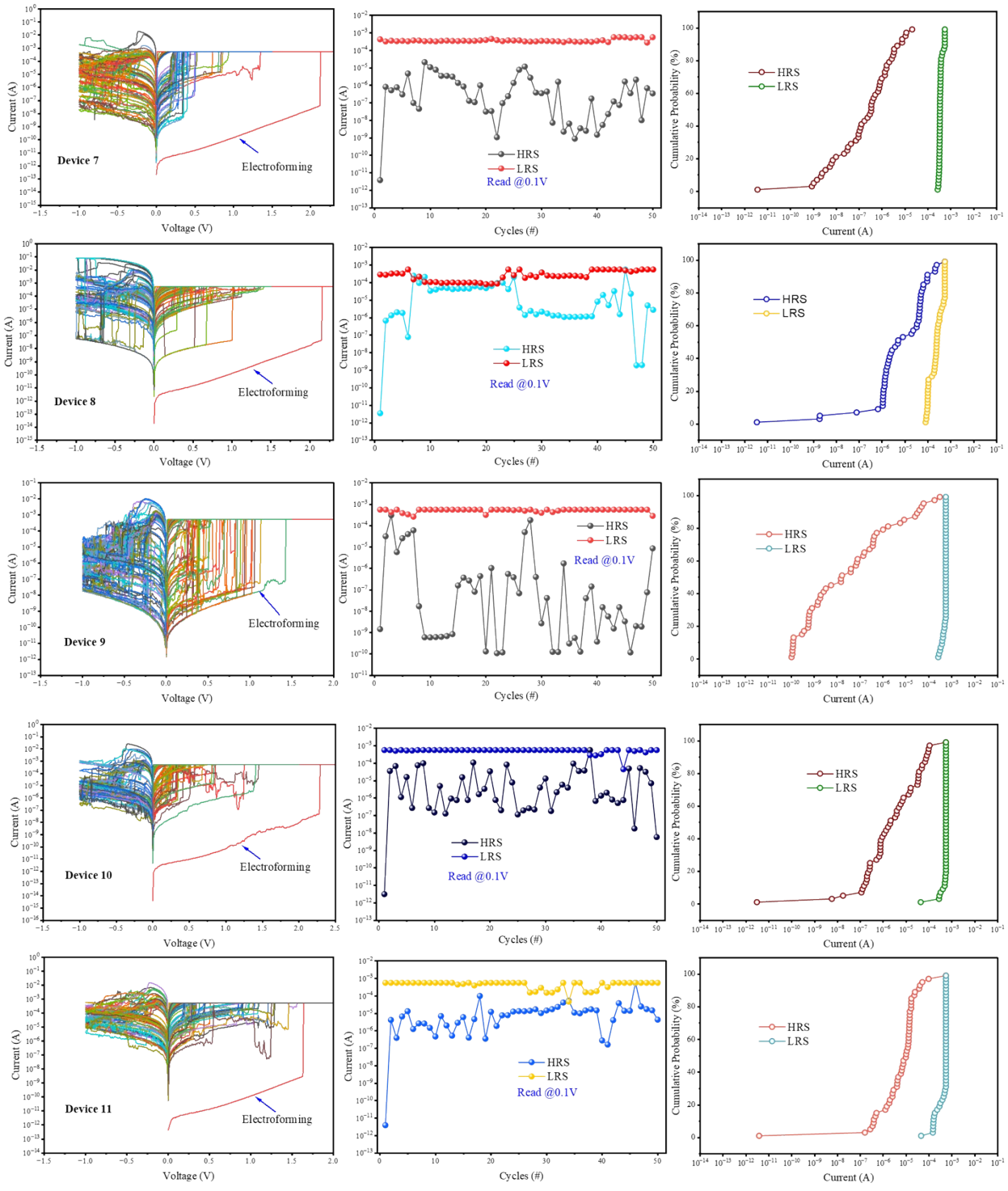

Figure S4: Electrical characteristics of the single-layer Pt/ZrO_2/Ag devices measured across 11 devices are presented. Consecutive I-V switching cycles show noticeable variability in switching voltages and current levels. The endurance measurements indicate fluctuating resistance states with limited separation between the HRS and LRS.

For Pt/NbOx/Ag (>10 Devices)

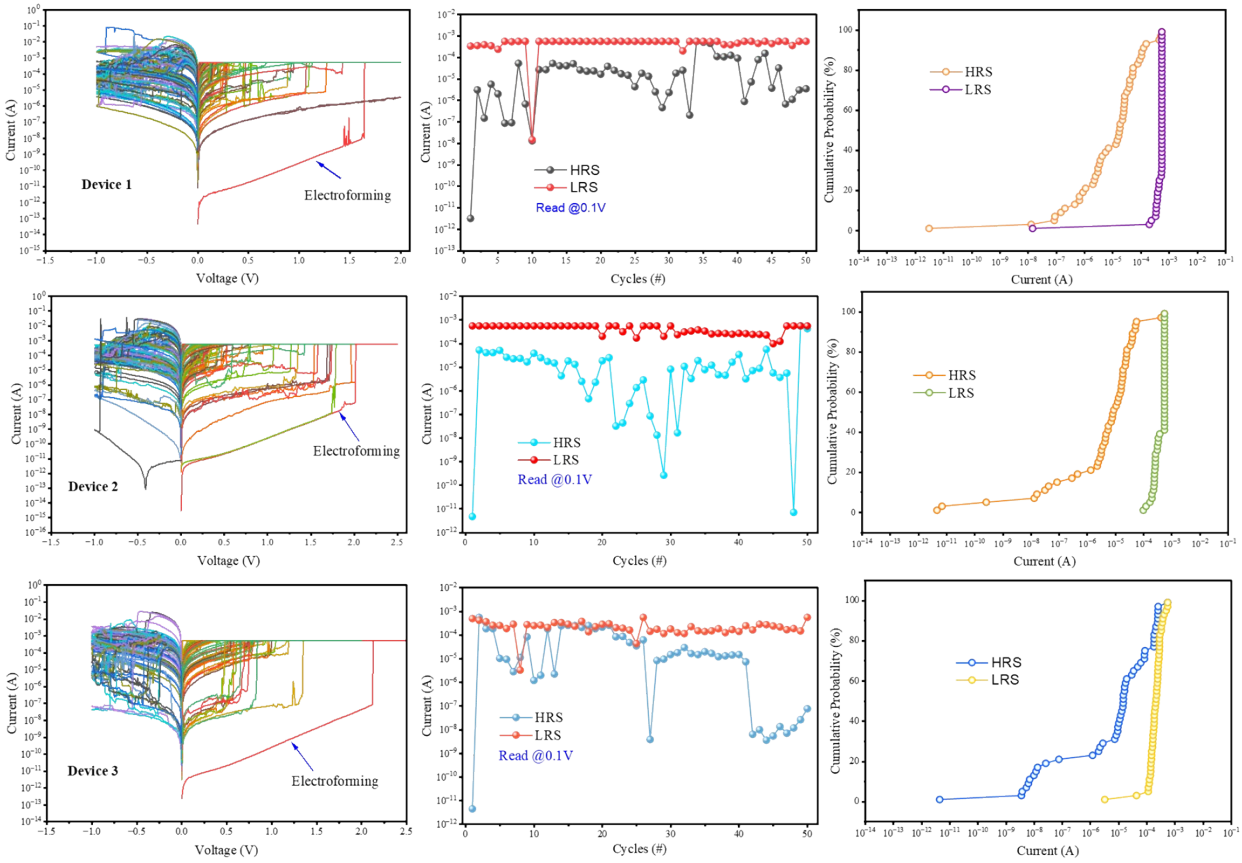

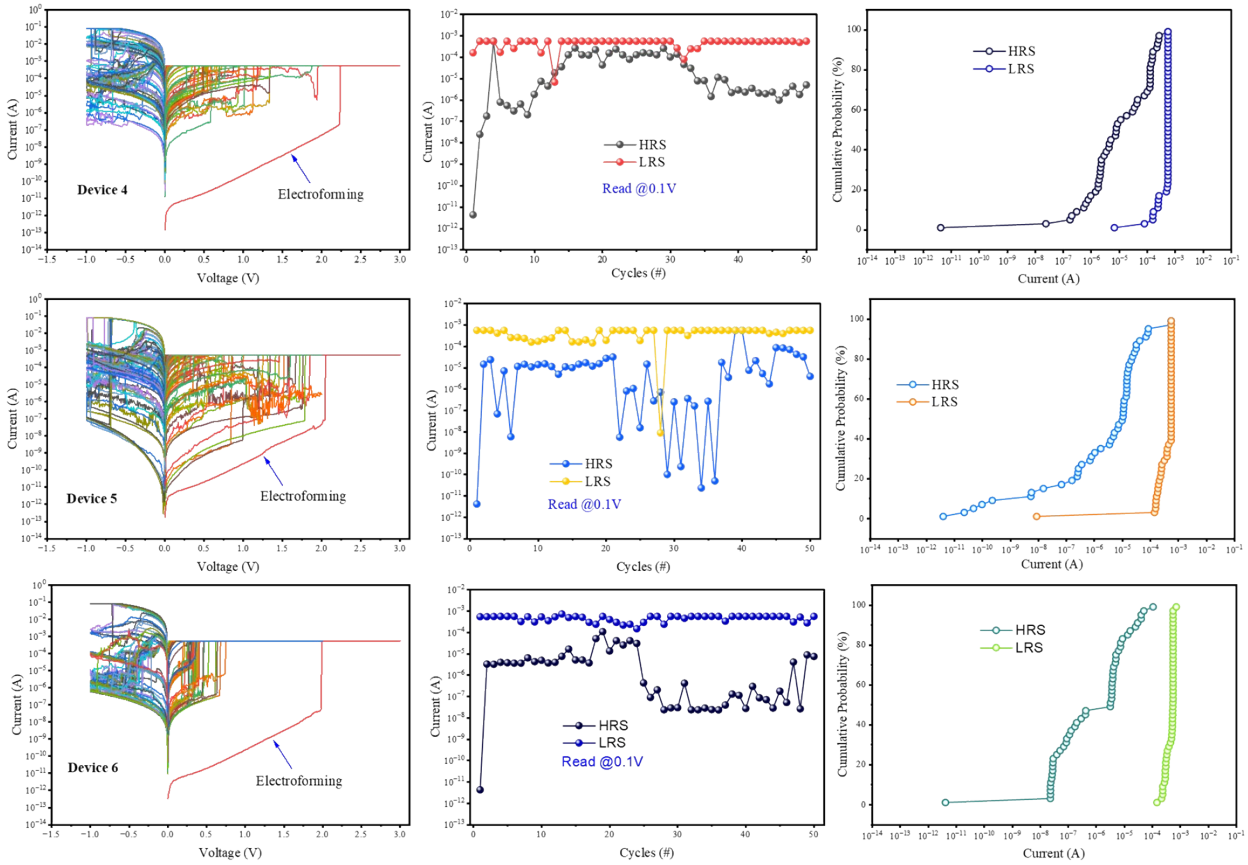
Device 4
Electroforming
Current (A)
Voltage (V)
HRS
LRS
Read @0.1V
Cycles (#)
Cumulative Probability (%)
Current (A)
Device 5
Electroforming
Current (A)
Voltage (V)
HRS
LRS
Read @0.1V
Cycles (#)
Cumulative Probability (%)
Current (A)
Device 6
Electroforming
Current (A)
Voltage (V)
HRS
LRS
Read @0.1V
Cycles (#)
Cumulative Probability (%)
Current (A)

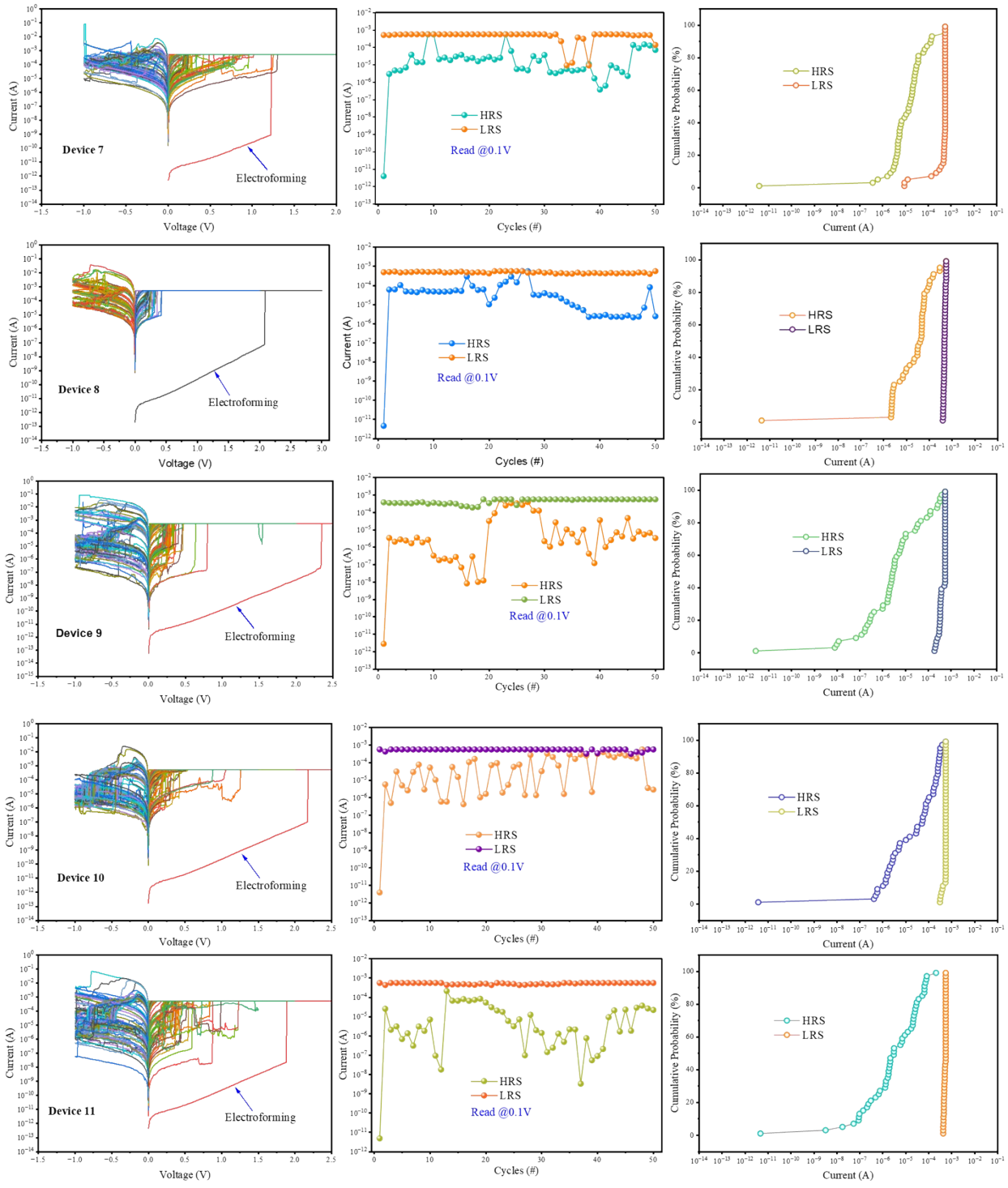

Figure S5: Electrical characteristics of the single-layer Pt/NbOx/Ag devices measured across 11 devices are presented. The electrical performance of the single-layer NbOx device is characterized by significant variability. Consecutive I-V switching cycles exhibit wide variations in threshold voltages and current levels, while the endurance characteristics reveal unstable resistance states

with large fluctuations between the HRS and LRS, confirming poor cycle-to-cycle reproducibility and highlighting the inherent instability of the single-layer structure.

In contrast to the single-layer devices, the Pt/NbOx/ZrO2/Ag bilayer memristor exhibits markedly improved switching uniformity and cycle-to-cycle stability.

For Bilayer Pt/NbOx/ZrO_2/Ag (>10 Devices)

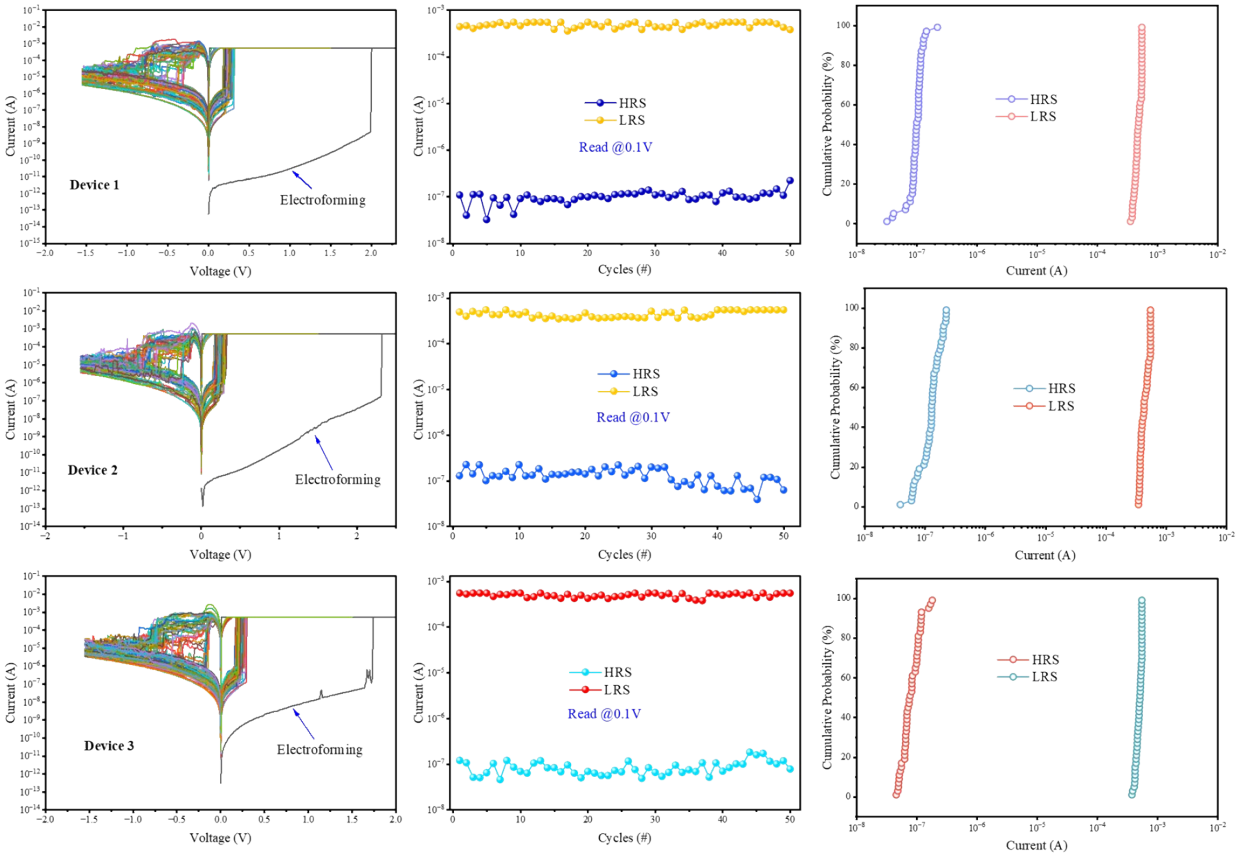

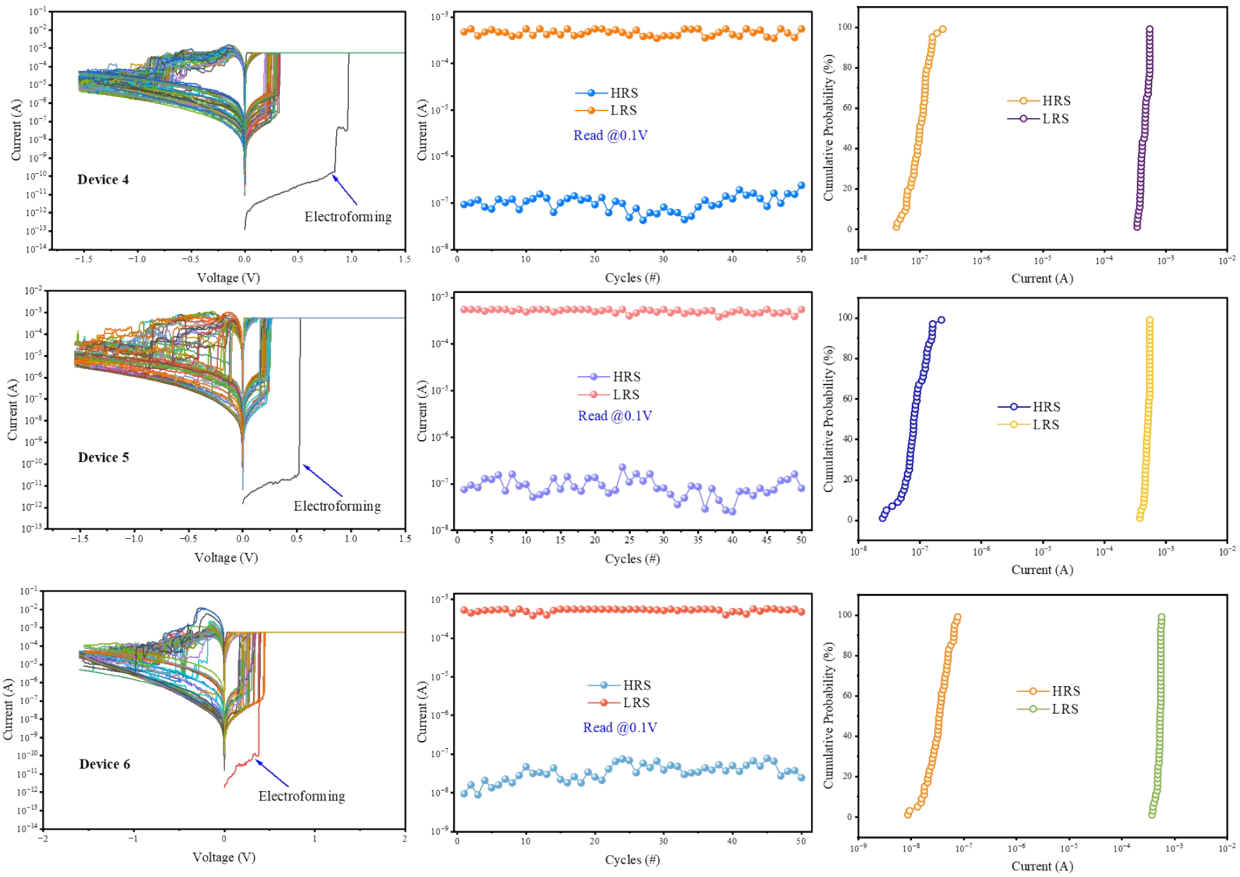
Device 4
Electroforming
Voltage (V)
Current (A)
HRS
LRS
Read @0.1V
Cycles (#)
Cumulative Probability (%)
Current (A)
Device 5
Electroforming
Voltage (V)
Current (A)
HRS
LRS
Read @0.1V
Cycles (#)
Cumulative Probability (%)
Current (A)
Device 6
Electroforming
Voltage (V)
Current (A)
HRS
LRS
Read @0.1V
Cycles (#)
Cumulative Probability (%)
Current (A)

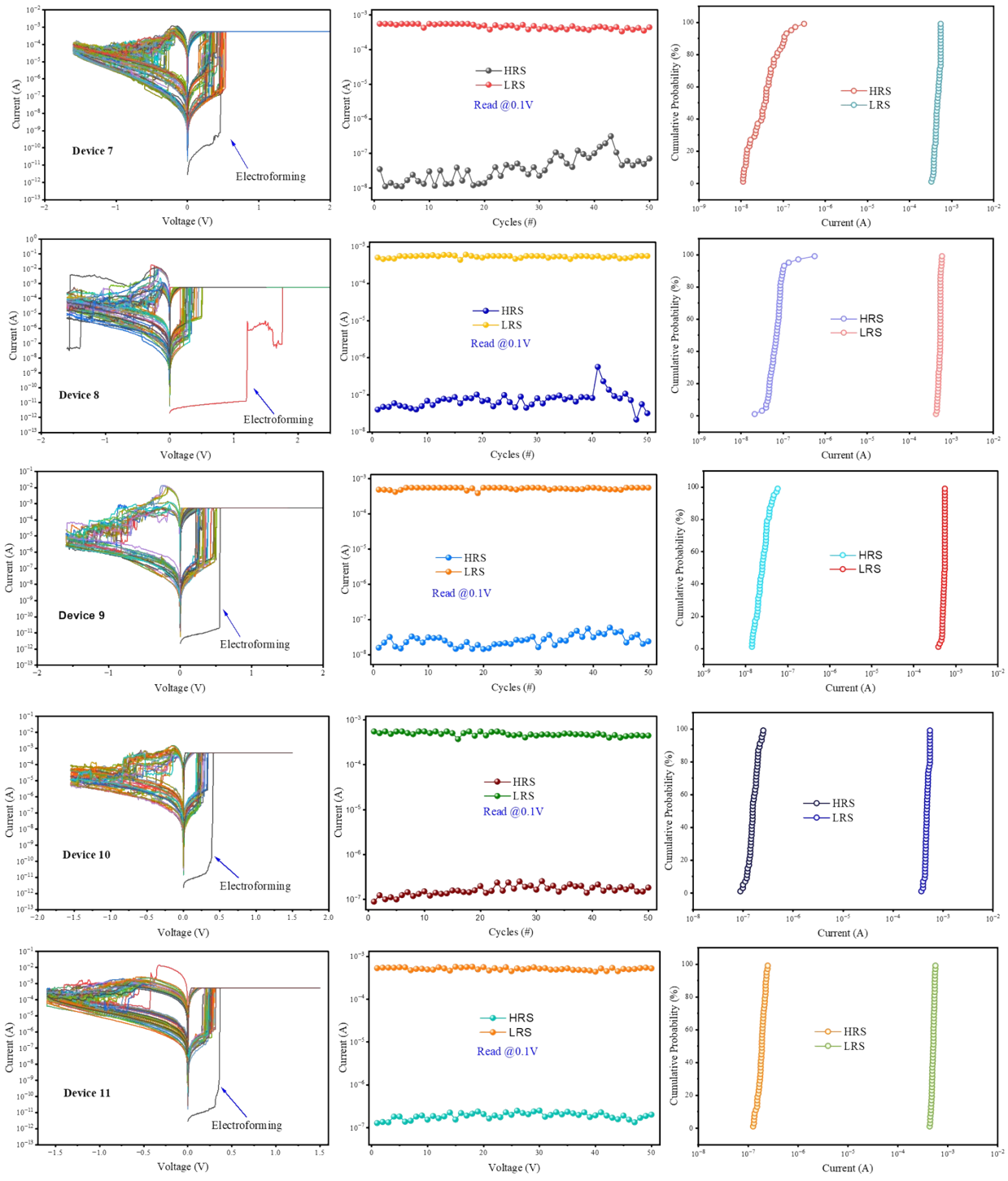

Figure S6: The electrical performance of the bilayer Pt/NbOx/ZrO2/Ag device demonstrates high stability and uniformity. Consecutive I-V switching cycles exhibit well-defined and repeatable threshold voltages with very low variation in current levels, while the endurance characteristics

show stable resistance states with clear separation between the HRS and LRS, confirming excellent cycle-to-cycle reproducibility and reliable switching behavior.

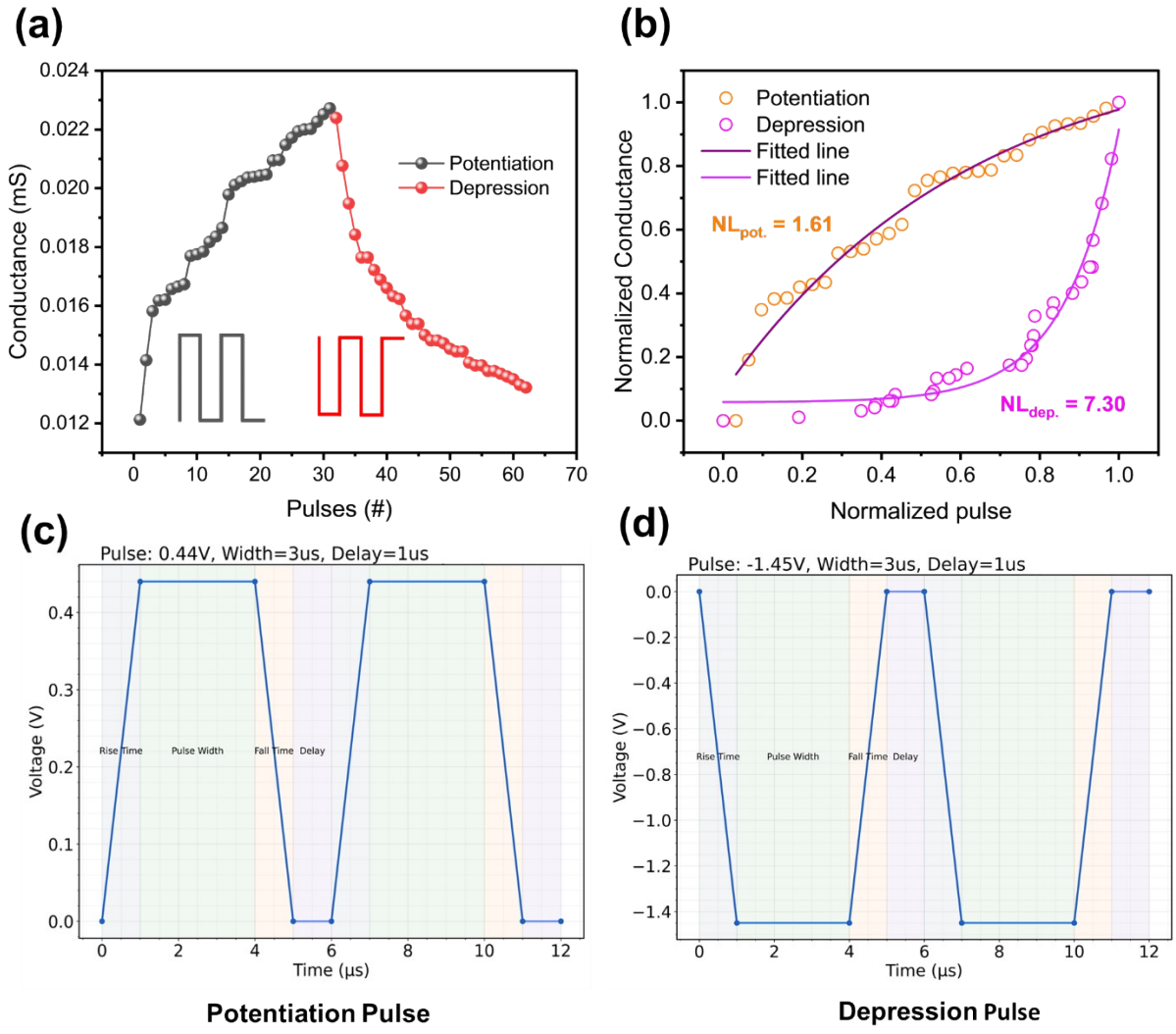

Figure S7: (a) Synaptic potentiation and depression characteristics under consecutive voltage pulses, and (b) corresponding normalized conductance curves and nonlinearity (NL) fitting. (c-d) Pulse schemes used for potentiation (+0.44 V) and depression (-1.45 V) operations, showing the rise, width, fall, and delay segments.

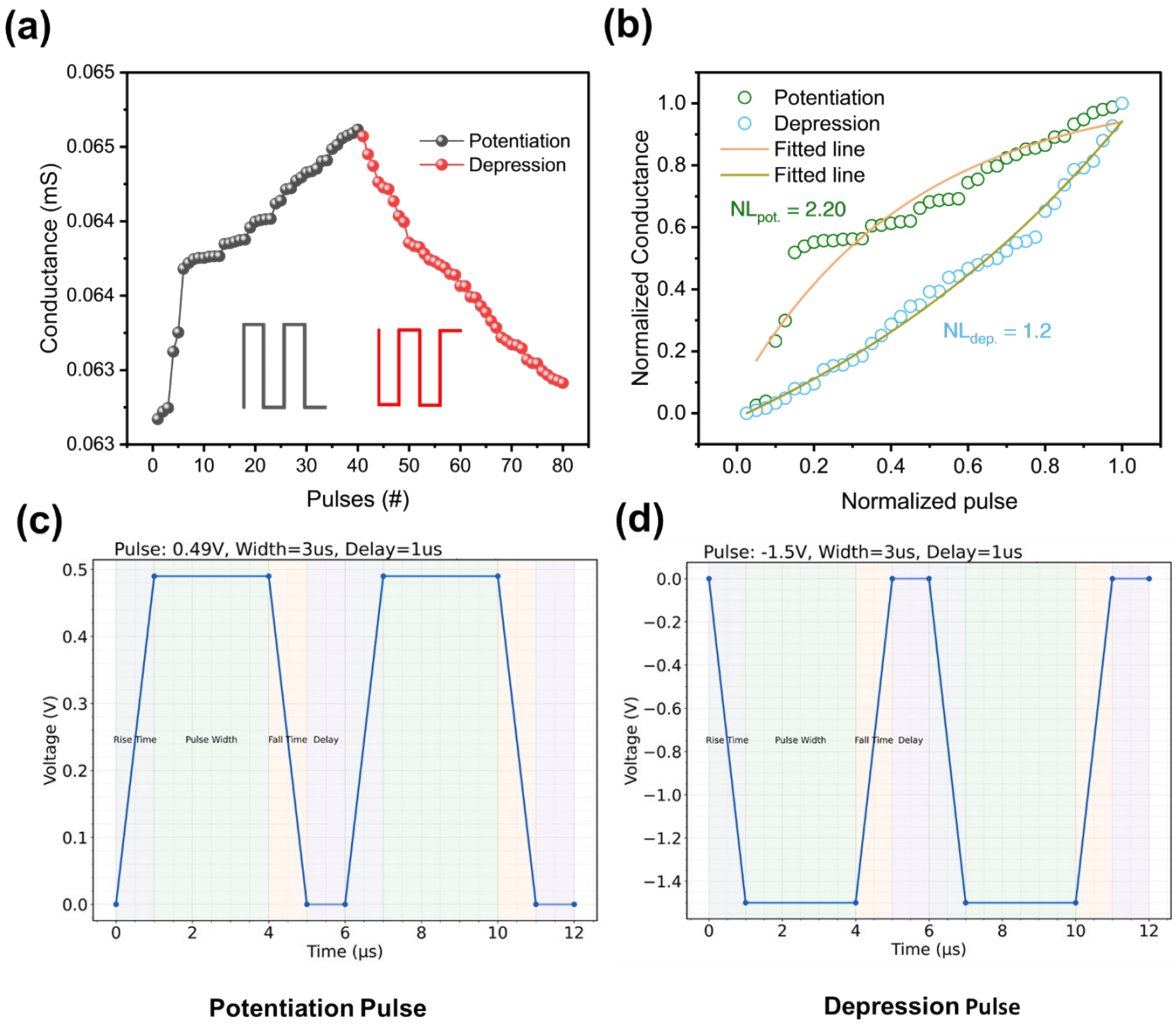

Figure S8: (a) Potentiation and depression characteristics of the device under different voltage amplitudes. (b) Conductance evolution with pulse number and corresponding nonlinearity fitting, (c-d) Applied positive (+0.49V) and negative (-1.5V) pulse waveforms for potentiation and depression with defined rise/fall time, width, and delay.

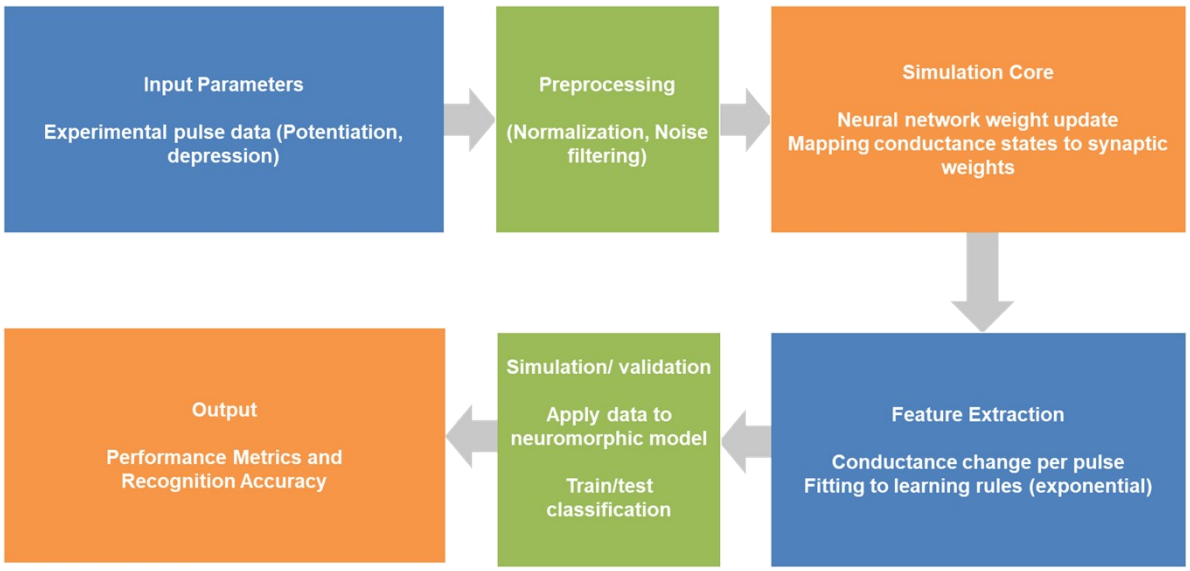

Figure S9: Flow chart of the neuromorphic simulation framework illustrating how experimentally measured potentiation and depression pulse data are processed and mapped to synaptic weights. The conductance states extracted from device measurements are normalized and fitted to learning rules, then directly translated into neural network weight updates within the simulation core, followed by validation and performance evaluation.

Head Mode	NC-AFM
Source	Topography
Data Width	256 (pxl)
Data Height	256 (pxl)
X Scan Size	5 (µm)
Y Scan Size	5 (µm)
Scan Rate	0.5 (Hz)
Z Servo Gain	2
Set Point	11 (nm)
Amplitude	14.98 (nm)
Sel. Frequency	296.92E3 (Hz)
Drive	14.83 (%)

Table S1: AFM topography image of the sample surface acquired in non-contact mode over a 5 × 5 μm^2 area. The table summarizes the key scan parameters and experimental conditions used during AFM measurement.

Device Structure	Conduction Type	Set/Reset Voltage (V)	Switching Type	Neural Network Performance	Key Summary	Ref.
$Au/Al_2O_3/MoS_2/Ti/Cu$	ECM	0.4/-0.6	Analog	Digit recognition	Copper-migration-controlled ECM memristor exhibiting multilevel switching behavior and synaptic weight modulation under controlled programming conditions.	1
$Pt/Ta_2O_5/SiO_2/Ag$	ECM	0.5/-1.0	Digital	N/A	Heterojunction device demonstrating low-voltage resistive switching with improved stability via heterojunction-assisted filament control.	2
$ITO/HfZnO_x/Ti/Au$	VCM	2.5/-2.5	Digital	Synapse	Stable 4-level multistate switching with reproducible endurance, demonstrating potentiation, depression, and forgetting through oxygen vacancy modulation	3
$Pt/HfO_2/Ag$	ECM	0.20/-0.4	Digital	Neuromorphic timing application	Ag-based diffusive ECM memristor investigating threshold switching and filament relaxation dynamics under pulsed operation, relevant for selector and neuromorphic timing applications.	4
ITO/PMMA/i-ITS/Au	ECM	4.0/-5.0	Digital	N/A	Organic ECM memristor employing interfacial triggering to localize metallic filament growth, enabling improved switching uniformity and flexible-device operation.	5

$Pt/Al_2O_3/NbO_x/Al$	VCM	2.0/-3.0	Analog	Pattern recognition	Forming-free analog switching with $>10^3$ endurance cycles and implementation of reservoir computing with high pattern recognition accuracy.	[6]
$Pt/NbOx/ZrO_2/Ag$	ECM	0.22/-0.15	Digital	F-MNIST recognition, LTP and LTD and PPF	Low-voltage well-defined bilayer memristor with high endurance, large ON/OFF ratio and tunable multilevel states, demonstrating LTP, LTD, PPF and FMNIST recognition.	This work*

Table S2: Comparison of bilayer memristor devices highlighting their switching characteristics and neuromorphic performance.

References

1. W. Ahn, H. B. Jeong, J. Oh, W. Hong, J. H. Cha, H. Y. Jeong and S. Y. Choi, *Small*, 2023, **19**, 2300223.
2. X. Guo, Q. Wang, X. Lv, H. Yang, K. Sun, D. Yang, H. Zhang, T. Hasegawa and D. He, *Nanoscale*, 2020, **12**, 4320-4327.
3. M. K. Hota, M. N. Hedhili, N. Wehbe, M. A. McLachlan and H. N. Alshareef, *Advanced Materials Interfaces*, 2016, **3**, 1600192.
4. S. A. Chekol, S. Menzel, R. W. Ahmad, R. Waser and S. Hoffmann-Eifert, *Advanced Functional Materials*, 2022, **32**, 2111242.
5. S.-H. Lee, H.-L. Park, M.-H. Kim, S. Kang and S.-D. Lee, *ACS Applied Materials & Interfaces*, 2019, **11**, 30108-30115.
6. D. Ju, H. Ji, J. Lee and S. Kim, *APL Materials*, 2024, **12**.